

# The weight of the mountains: Constraints on tectonic stress, friction, and fluid pressure in the 2008 Wenchuan earthquake from estimates of topographic loading

Richard H. Styron<sup>1</sup> and Eric A. Hetland<sup>1</sup>

**Abstract.** Though it is widely recognized that large mountain ranges produce significant stresses in the Earth's crust, these stresses are not commonly quantified. Nonetheless, near large mountains topography may affect fault activity by changing the stress balance on the faults. In this work, we calculate the stress field from topography in the Longmen Shan (Sichuan, China) and resolve those stresses on several models of the faults that ruptured in the 2008  $M_w$  7.9 Wenchuan earthquake. We find that the topography results in shear stresses up to 20 MPa and normal stresses up to 80 MPa on the faults, with significant variability across the faults. Topographic stresses generally load the fault in a normal and left-lateral shear sense, opposite to the inferred coseismic slip sense, and thus inhibit the coseismic slip. We estimate the accumulated tectonic stress needed to overcome topographic and lithostatic stresses so that the direction of maximum shear on the faults is roughly collinear with the inferred coseismic slip. We further estimate the static friction and pore fluid pressure assuming that the fault was at Mohr-Coulomb failure at the time of the Wenchuan earthquake. We use a Bayesian inversion strategy, yielding posterior probability distributions for the estimated parameters. We find most likely estimates of maximum tectonic compressive stress near  $0.6 \rho g z$  and oriented ~E-W, and minimum tectonic stress near  $0.2 \rho g z$ . Static friction on the fault is near 0.2, and pore fluid pressure is between 0 and 0.4 of the total lithostatic pressure.

## 1. Introduction

"And He has set up on the earth mountains standing firm, lest it should shake with you" – *The Holy Qur'an*, 15:16

Stress is of fundamental importance to many processes in the earth. Both the isotropic and deviatoric components of stress exert control on the deformation state of the earth at any point in the brittle regime. However, unlike other fundamental quantities such as temperature, stress is typically difficult to measure *in situ*, without drilling-based techniques. Therefore, stress is often treated in a semi-quantitative manner, with an emphasis on directions and relative magnitudes of the principal stresses, either locally or regionally [e.g., *Angelier*, 1994]. These estimates of stress are commonly derived from strain, for example from studies of earthquake focal mechanisms [e.g., *Michael*, 1987] or of fault slip data [e.g., *Reches*, 1987; *Medina Luna and Hetland*, 2013].

In areas of substantial relief, high terrain and steep slopes generate large stresses in the crust beneath and adjacent to the high topography [Jeffreys, 1924; Coblenz and Richardson, 1996]. Because of the irregularity of topography in mountainous regions, the stresses produced by topography are also heterogeneous, and may play a prominent role in local or regional deformation, particularly if the region is tectonically active. For example, shear and normal stresses on a fault from topographic loading may push a particular fault closer to or (as suggested by the Qur'an) farther from failure, or reorient the net shear stress direction on a fault. These effects may affect the localization or deformational style in a region. Furthermore, heterogeneous topographic stresses on a particular fault may affect the way earthquake ruptures propagate across the fault plane. Despite this, the degree to which topographic stresses affect faulting has received little direct study.

In this work, we investigate the effects of topographic stresses on the faults that ruptured in the 2008  $M_7.9$  Wenchuan, China earthquake. This earthquake is an ideal candidate for this study because it occurred at the base of the Longmen Shan, one of the largest and steepest escarpments on Earth (Figure 1), and has a well-studied coseismic slip distribution characterized by significant along-strike variations in coseismic slip. Additionally, because the earthquake occurred after ~2000 years of seismic quiescence, post-seismic stresses in the lithosphere are likely to be negligible, suggesting that the stress state on the faults at the time of rupture can be approximated as the sum of topographic, lithostatic, and accumulated tectonic stresses. We then use the Mohr-Coulomb failure criterion to bracket the tectonic stress field, pore fluid pressure, and static friction of the fault.

### 1.1. Previous work on topographic stresses

Aspects of topographic stresses and their relevance to tectonics have been studied for some time. Jeffreys [1924] noted that the presence of high mountains is evidence that the Earth's crust can support significant heterogeneous differential stresses over long time periods. Dalmayrac and Molnar [1981] and Molnar and Lyon-Caen [1988] discussed how extensional deformation in the high parts of orogens that is temporally coincident with contractional deformation at the low-elevation margins of the orogen may be explained by a spatially invariant, depth-integrated horizontal compressive stress with spatially varying vertical stresses caused by topography. Richardson and Coblenz [1994] exploited this relationship in the central Andes to estimate horizontal tectonic stresses through finite element modeling, and more recently Copley *et al.* [2009] performed similar work in Albania. Bollinger *et al.* [2004] showed how increased normal stress on the Main Himalayan thrust due to loading of the high Himalayan massifs locally suppressed microseismicity and increased fault locking. Meade and Conrad [2008] demonstrated that the increased weight of the uplifting Andes influenced the Nazca-South America convergence rate.

Additionally, topographic stresses play a role in common models of orogenic dynamics. For example, topographic loading is

<sup>1</sup>Department of Earth and Environmental Sciences, University of Michigan, Ann Arbor, Michigan, USA.

central to thin viscous sheet models of lithospheric deformation [e.g., *Bird and Piper*, 1980; *Flesch and Kreemer*, 2010]. Critical taper models for thrust or extensional wedges [e.g., *Dahlen*, 1990; *Xiao et al.*, 1991] incorporate both variation in vertical stress due to changing elevation as well as a shear stress contributed by the slope of the wedge surface. Critical taper models also incorporate the idea that in a growing wedge, progressively increasing topographic stresses may eventually prevent continued slip on a given fault plane, and strain will instead be transferred to the toe of the thrust wedge where the stress state is more favorable. Of particular relevance to our work are ‘fixed boundary’ models of gravitational collapse and spreading [*Rey et al.*, 2001], where an excess of gravitational potential energy associated with the high topography and thickened crust of eastern Tibet causes a transfer of rock to the foreland through horizontal contraction at the rangefront [e.g., *Dewey*, 1988; *Liu and Yang*, 2003; *Copley and McKenzie*, 2007]. This process may be aided by a weak (sub)horizontal structure at depth (such as a shear zone or weak crustal channel) that is capable of transferring the vertical and radial stresses from topography throughout an orogen to its margins, leading to contraction there [e.g., *Clark et al.*, 2005; *Burchfiel et al.*, 2008; *Flesch and Bendick*, 2012].

The contributions of variable topography to the full stress field in the elastic upper crust has been studied on smaller spatial scales. *McTigue and Mei* [1981] and *Savage and Swolfs* [1986] investigated the stress components from long, symmetric ridges and showed how horizontal tension is induced under ridge crests and horizontal compression is induced under valleys, mostly due to shear stresses generated by slopes. Work in this vein was continued by *Miller and Dunne* [1996] and *Martel* [2006], who have focused on shallow rock fracturing resulting from topographic stresses. *Liu and Zoback* [1992] investigated whether the topographic stresses generated by the mountains around Cajon Pass (California, USA) contributed to the observed left-lateral shear stress on a shallow

portion of the right-lateral San Andreas fault. In their study, they developed methods for calculating the three dimensional elastic stress tensor field arbitrary topography, whereas previous solutions were limited to two dimensions and required topography to be mathematically-defined (e.g., sinusoidal).

*Luttrell et al.* [2011] inferred the coseismic shear stress changes during the 2010  $Mw8.8$  Maule, Chile earthquake, and using the topographic stresses due to the overlying fore arc, constrained the the stresses that led to this earthquake. In their study, they calculated topographic stresses following a similar procedure as *Liu and Zoback* [1992] (which we describe below), although they only considered the component of the topographic load that can be described by convolving a Boussinesq solution with the topography. *Luttrell et al.* [2011] also considered the contribution to stresses due to buoyancy.

## 1.2. The 2008 Wenchuan, China earthquake

The 2008  $M7.9$  Wenchuan, China earthquake is one of the most devastating earthquakes in recent history (for an in-depth review and discussion of the earthquake, see *Zhang et al.* [2010]). Surface rupture occurred along a 240 km segment of the Beichuan fault and a parallel 72 km segment of the Pengguan fault [*Xu et al.*, 2009] (Figure 1). These faults lie at the base of the central and northeastern Longmen Shan, a mountain range that forms the eastern margin of the Tibetan plateau. Total relief across the central Longmen Shan is around 4 km, though relief subsides somewhat to the northeast. The central and southwestern Longmen Shan is the steepest margin of the Tibetan plateau [*Clark and Royden*, 2000] and one of the highest and steepest escarpments on earth. This is most apparent in the southwestern portion of the earthquake rupture, where elevations  $> 4000$  m over the Pengguan massif (a Precambrian crystalline massif in the hanging wall of the Beichuan thrust) drop to  $\sim 1200$  m in as little as 6 km map distance.

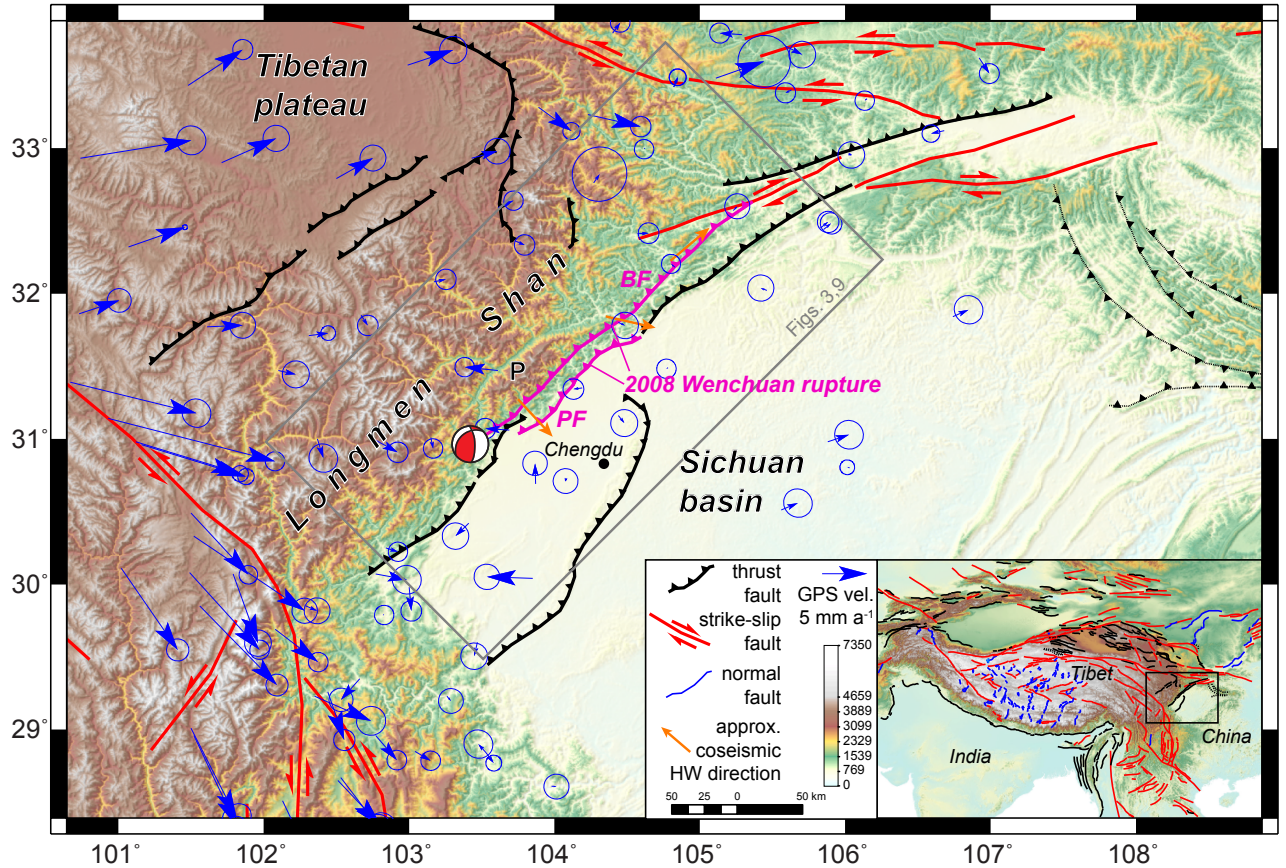


**Figure 1.** Map of eastern Tibet and the Sichuan basin, showing active structures from Styron *et al.* [2010]. Faults that ruptured in the 2008 Wenchuan earthquake are shown in pink. GPS velocities are relative to the mean velocity of sites within Sichuan basin, with  $1\sigma$  uncertainty, from the dataset of Liang *et al.* Liang *et al.* [2013]. Beachball is from the Global CMT focal mechanism solution for the 2008 Wenchuan earthquake. BF = Beichuan fault. PF = Pengguan fault. P = Pengguan massif. Grey box shows the extent of Figures 3 and 9.

Surface ruptures during the Wenchuan earthquake are highly variable and show vertical (reverse-sense) displacements up to 9 m and horizontal (right-lateral sense) displacements up to 5 m [Lin *et al.*, 2009; Liu-Zeng *et al.*, 2009; Xu *et al.*, 2009]. In general, vertical displacements are higher in the southwestern to central portions of the Beichuan rupture and decrease in the northeast, whereas horizontal offsets are higher in the central to northeast, though considerable variation exists. Coseismic slip models constrained by seismic and geodetic data reveal a complicated pattern of coseismic slip in the Wenchuan earthquake, with several high-slip patches that dominate the seismic moment release and significant variation coseismic slip rake along strike [e.g., Nakamura *et al.*, 2010; Shen *et al.*, 2009; Tong *et al.*, 2010; Feng *et al.*, 2010; Zhang *et al.*, 2011; Qi *et al.*,

2011; Fielding *et al.*, 2013]. The variation in rake is such that the southwest portions of the fault slipped largely in a reverse sense, while the northeast portions slipped largely in a right-lateral sense. This change in rake is associated with a change in inferred fault dip. Sections of faults that ruptured in the Wenchuan earthquake (which we simply refer to as the “Wenchuan earthquake faults”) with shallow to moderate dips largely ruptured as thrust, and sections with steeper dips largely ruptured as strike-slip. Medina Luna and Hetland [2013] concluded that this relationship is consistent with a uniform orientation of principal stresses, where the variation of the dip of the fault leads to a change in the direction of maximum fault shear stress, which they assumed to be parallel to the coseismic slip rake.

### 1.3. This study

We seek to quantify the topographic stress field in the Longmen Shan region, and on the Wenchuan earthquake faults themselves. Specifically, we evaluate the extent to which topographic stresses promote or inhibit slip in the 2008 Wenchuan earthquake. If topographically induced shear stresses on the fault are in roughly in the same direction as the coseismic slip, then topographic loading general promotes coseismic slip (Figure 2 a). On the other hand, if the topographic shear stresses are roughly in the opposite direction of coseismic slip, then topographic loading inhibits coseismic slip (Figure 2 b). If topographic loading resisted slip across the Beichuan faults, then tectonic stresses would need to counteract the topographic fault stresses for the coseismic slip to result. On a smaller scale, the heterogeneity of coseismic slip in the earthquake may be influenced by shorter wavelength variations in topography and topographic stresses.

Topographic stresses are only one component of the total stress field in the crust [Molnar and Lyon-Caen, 1988]. Coseismic slip in the Wenchuan earthquake is due to the total accumulated stress on the faults, which also includes components from lithostatic and tectonic stresses. (In the present study, we do not consider stresses due to flexure [e.g., Luttrell *et al.*, 2007] or buoyancy [e.g., Luttrell *et al.*, 2011].) By quantifying both the topographic and lithostatic stresses, we can use coseismic slip models to solve for the tectonic stress assuming that (1) the total shear stress on the fault is in the direction of coseismic slip [e.g., Angelier, 1994] and (2) the fault is at Mohr-Coulomb failure everywhere that it slipped. If topographic stresses are significant and produce shear in the direction of fault slip, then for given values of static friction and pore fluid pressure, we can calculate the amount of tectonic stress that can be added to the ambient stress field before the faults should rupture; given limited acceptable ranges for friction and fluid pressure, we are essentially able to place maximum constraints on tectonic stress. Alternately, if topographic stresses work against coseismic slip, for given friction and fluid pressures we can estimate the minimum magnitudes of tectonic stresses necessary to overcome shear and frictional resistance to slip. In a scenario with complex faulting and topography, it may be possible to put tight bounds on minimum and maximum magnitudes and directions of tectonic stresses. To account for the non-uniqueness of the solution, we use a Bayesian Monte-Carlo methodology to estimate posterior probability density functions (PDFs) of tectonic stresses, static fault friction, and pore fluid pressure.

## 2. Topographic stresses on the Longmen Shan faults

To quantify tectonic stresses on the Wenchuan earthquake faults, we first calculate the topographic stress field in the upper crust throughout eastern Tibet, then interpolate those stresses onto three dimensional models of the faults taken from coseismic slip models. Finally, we calculate topo-

graphic shear and normal stresses on the faults and compare those to the coseismic slip patterns.

### 2.1. Topographic stress tensor field calculations

We calculate the stress tensor field induced by topography throughout eastern Tibet using methods developed by Liu and Zoback [1992]. They show that the topographic stress tensor field can be determined by a convolution of topographic loading functions with Green's functions describing the stresses in an elastic halfspace due to a point load at the surface. In our notation, the stress tensor field due to topography is given by

$$M(x, y, z) = G(x, y, z) * F(x, y), \quad (1)$$

where  $G(x, y, z)$  is a set of Green's functions for the six stress tensor elements, and  $F(x, y)$  is a topographic loading function, described below. We assume compressive stresses are positive, and  $x > 0$  is east,  $y >$  is north, and  $z > 0$  is depth. Liu and Zoback [1992] show that  $M(x, y, z)$  can be decomposed into two components as

$$M(x, y, z) = M^B(x, y, z) + M^C(x, y, z). \quad (2)$$

$M^B(x, y, z)$  is the component of the stress field due to the vertical loading of the topography, and is

$$M^B(x, y, z) = G^B(x, y, z) * F_v(x, y), \quad (3)$$

where  $G^B(x, y, z)$  are the Boussinesq solutions for stresses in a halfspace due to a vertical point load on the surface (see Appendix A1),  $F_v(x, y) = \rho g h(x, y)$ , and  $h(x, y)$  is topography. Note that  $h(x, y) < 0$  since  $z < 0$  is depth.  $M^C(x, y, z)$  is the component of the stress field due to the mechanical coupling of the topography to the half-space, i.e., describing the lateral spreading forces in the rock above the halfspace, and is given by

$$M^C(x, y, z) = G_x^C(x, y, z) * F_{h,x}(x, y) + G_y^C(x, y, z) * F_{h,y}(x, y), \quad (4)$$

where  $G_i^C(x, y, z)$  are the Cerruti solutions for a horizontal point source load in the  $i$  direction on the halfspace surface (see Appendix A1). The horizontal loading functions are given by

$$\begin{aligned} F_{h,x}(x, y) = & (\rho g h(x, y) + M_{xx}^B(x, y, 0) + T_{xx}) \frac{\partial h}{\partial x} \\ & + (M_{xy}^B(x, y, 0) + T_{xy}) \frac{\partial h}{\partial y} \end{aligned} \quad (5)$$

and

$$\begin{aligned} F_{h,yz}(x, y) = & (\rho g h(x, y) + \sigma_{yy}^B(x, y, 0) + T_{yy}) \frac{\partial h}{\partial y} \\ & + (M_{xy}^B(x, y, 0) + T_{xy}) \frac{\partial h}{\partial x}. \end{aligned} \quad (6)$$

$M_{ij}^B(x, y, 0)$  is the stress from the vertical (Boussinesq) load evaluated at  $z = 0$ , and  $T_{ij}$  is the tectonic stress component, which we neglect in the present calculations.

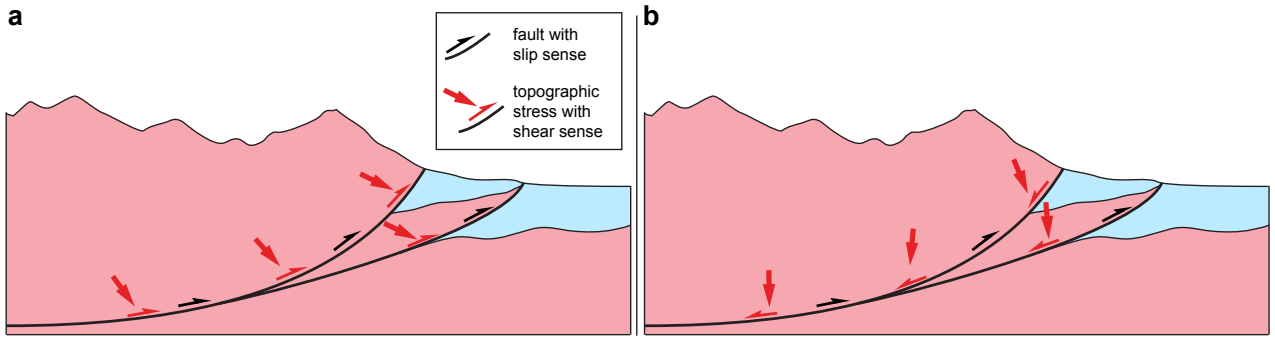


**Figure 2.** Scenarios for topographic effects on rangefront thrust faulting. (a) Topographic stresses promote thrust faulting. (b) Topographic stresses inhibit thrust faulting.

## 2.2. Numerical implementation

Topography was taken from the CGIAR-CSI v.4 release [Jarvis *et al.*, 2008] of the Shuttle Radar Topographic Mission [Farr *et al.*, 2007] Digital Elevation Model (DEM) at 1 km nominal resolution. The DEM was projected from native WGS84 geographic coordinates to UTM zone 48N, decreasing the nominal horizontal resolution to 851 m. We assume a Poisson halfspace, and Green's functions for the Boussinesq and Cerruti point-source solutions were calculated at regular points in large 2-D grid at each depth considered, with the point-source centered in the grid (see Table 1 for model parameters). A mask was applied to each of the discretized Green's functions such that values outside a radius (i.e. the ‘corners’ of the array) were set to zero, yielding a circular array. The size of the grid was chosen to be quite large to incorporate potential contributions from the elevated topography throughout eastern Tibet. So that the Green's functions and the topography were discretized on the same size grid, we pad the Green's function array with zeros. Because of singularities in the Green's functions at  $z = 0$ , we use  $\sigma^B(x, y, z)$  with  $z = 851$  m, the shallowest level of our calculations, in construction of the horizontal loading functions in Equations 5 and 6. Convolutions were computed using a 2D fast Fourier transform. All calculations were implemented in Python (v. 2.7.3) using IPython [Pérez and Granger, 2007], NumPy (v. 1.7) [Oliphant, 2007] and Pandas (v. 12) [McKinney, 2010]; additional statistical analysis was performed with StatsModels [Seabold and Perktold, 2010]. We created an open-source Python package to calculate topographic stresses in a reasonably automated way, which is available at <https://github.com/cossatot/halfspace>. The package is being expanded to encompass a wide range of elastic stress and strain solutions as time permits. All data and scripts for this particular project are available at [https://github.com/cossatot/wenchuan\\_topo\\_stress](https://github.com/cossatot/wenchuan_topo_stress).

## 2.3. Topographic fault stress calculations

Topographic stresses on the Wenchuan faults are calculated on point sets representing the faults taken from coseismic slip models. We use the coseismic slip models of Shen *et al.* [2009], Feng *et al.* [2010], Qi *et al.* [2011], Zhang *et al.* [2011], and Fielding *et al.* [2013], and discard points above 851 m below sea level, as this is above the depth at which we compute  $G^C(x, y, z)$ . The six stress tensor com-

ponents calculated at the regular grid points are linearly interpolated to points describing the faults. Because the fault points are completely surrounded by the grid nodes at which topographic stresses were calculated and those nodes are spaced  $<1$  km apart, the fault points cannot be more than a few hundred meters from the nearest grid node, so a higher order interpolation is not necessary. We then project the topographic stress tensor to fault normal stress,  $\sigma_n^M$ , down-dip shear stress,  $\tau_d^M$  and strike-slip shear stress,  $\tau_s^M$  at each point in describing the fault geometry.

## 3. Results of topographic stress calculations on the Wenchuan faults

Topographic stresses on the Wenchuan faults are on the order 1–10s MPa (Figure 3, 4). Stresses are highest in the southwest, beneath the Pengguan massif (the highest topography of the Longmen Shan front), and decrease to the northeast.  $M_{zz}$  is typically larger, though not substantially, than  $M_{xx}$  or  $M_{yy}$ . Maximum horizontal stress is not typically aligned with either cardinal horizontal direction, and is typically larger than  $M_{zz}$  above 10 km. Maximum  $M_{zz}$  is near 80 MPa, on the southwestern Beichuan fault below the high peaks of the Pengguan massif, except for in slip models containing near-horizontal fault segments in the mid-crust, where  $M_{zz}$  reaches 100 MPa. Vertical shear stresses ( $M_{xz}$  and  $M_{yz}$ ) are on the order of 1 MPa, and horizontal shear stress ( $M_{xy}$ ) is on the order of 0.1 MPa.

Because the compressive stresses are near equal,  $M$  contains a large isotropic component and a smaller deviatoric component. Consequently,  $M$  resolves on the Wenchuan faults with a large  $\sigma_n^M$  (median of about 40–60 MPa for each slip model) and much smaller  $\tau_d^M$ . The median  $\tau_d^M$  is about -3 to -6 MPa in each slip model, where values less than zero indicate normal-sense shear, and  $\tau_s^M$  median values range from about -2 to 1 MPa, where values less than zero indicate sinistral shear; fault models with positive median  $\tau_s^M$  have broad thrust flats at depth, where little slip occurred. On the steeper fault segments (where most of the moment release occurred), topographic shear stresses are typically normal-

sinistral, as opposed to the dominant mode of coseismic slip, which is reverse-dextral.

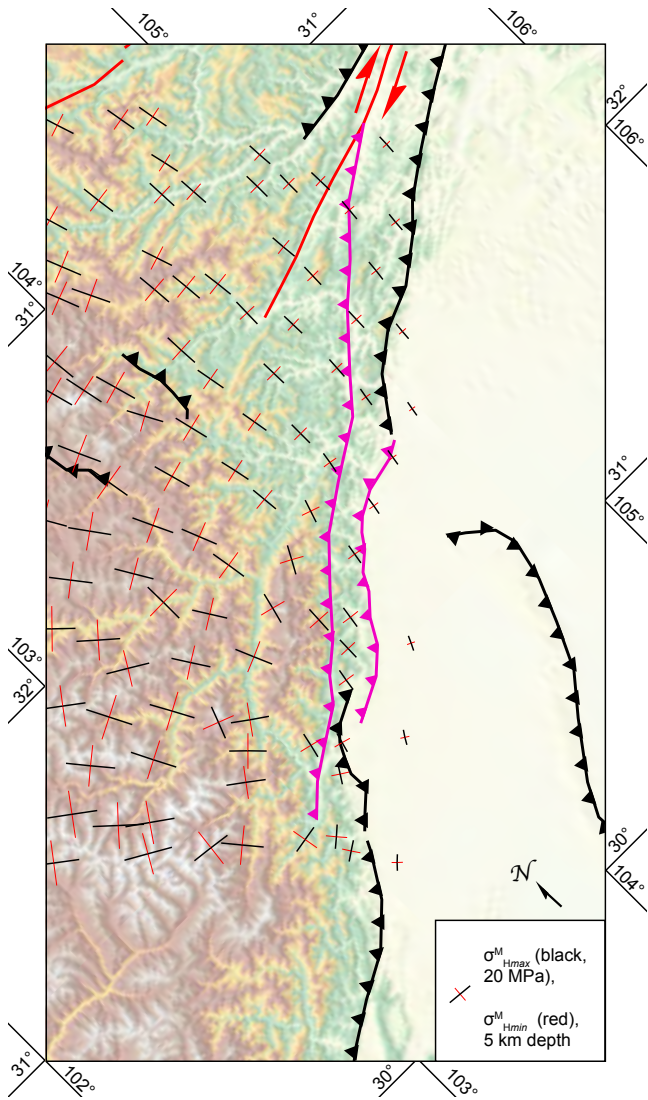


**Figure 3.** Horizontal topographic stresses in the Longmen Shan region at 5 km depth: black and red lines signify most and least compressive horizontal stresses, respectively. Other symbols are the same as in Figure 1. Stresses shown are down-sampled from the discretization used in the calculations by a factor of six.

**Table 1.** Parameters for numerical calculations of topographic stresses.

Parameter	Value	Unit
horizontal spacing	851	m
vertical spacing	1000	m
minimum depth	851	m (below sea level)
maximum depth	35851	m (below sea level)
density ( $\rho$ )	2700	$\text{kg m}^{-3}$
g	9.81	$\text{m s}^{-2}$
Green's function radius	9e5	m
Poisson ratio	0.25	-

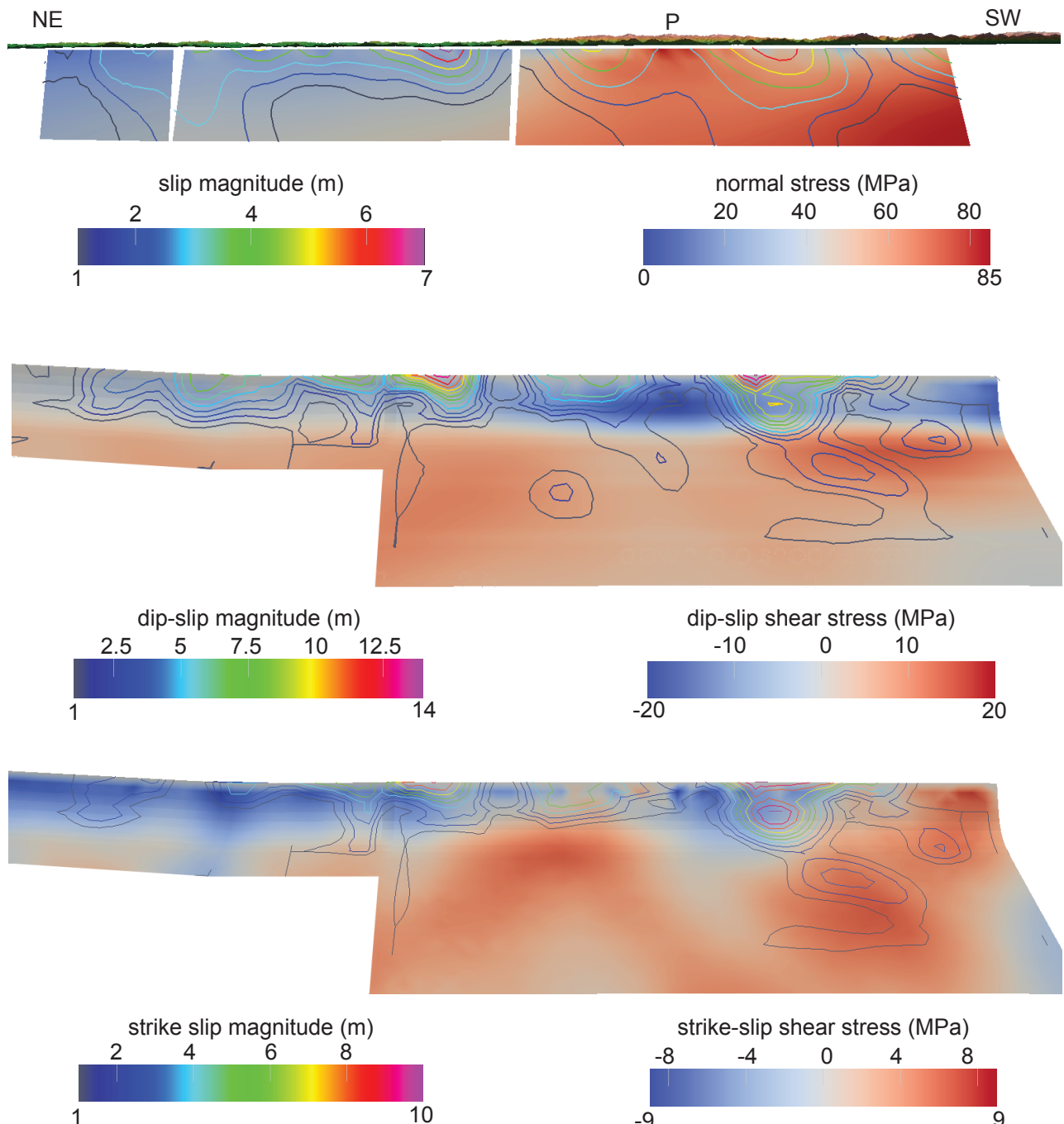


**Figure 4.** Southwest-looking views of topographic stresses and coseismic slip on selected slip models. All models share same lateral extent, but the perspectives for B and C are more inclined than A. (A)  $\sigma_n^M$  (colors), slip magnitude (contours, 1 m interval) and hanging-wall topography on the Feng *et al.* [2010] model of the Beichuan fault. Note the suppression of fault slip where normal stress is highest, such as below the Pengguan massif (P). Fault and topography share the same scale, with no vertical exaggeration. (B)  $\tau_d^M$  (colors) and dip slip (contours, 1 m interval) on the Qi *et al.* [2011] ‘rough’ slip model. (C)  $\tau_s^M$  (colors) and strike slip (contours, 1 m interval) on the Qi *et al.* [2011] slip model.

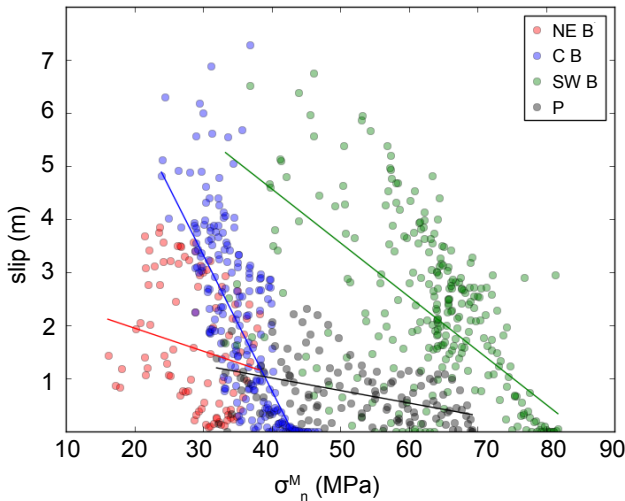


**Figure 5.** Coseismic slip magnitude and  $\sigma_n^M$  on the four segments of the Feng *et al.* [2010] coseismic slip model. Trendlines are L1 regressions and do not include points with no slip. “NE B” = Northeastern Beichuan fault. “C B” = central Beichuan fault. “SW B” = Southwestern Beichuan fault. “P” = Pengguan fault.

In contrast to the steeper fault segments, much of the shallowly-dipping fault segments (the Pengguan fault and flats at the base of the Beichuan fault, where present) have  $\tau^M$  in the direction of coseismic slip.  $M$  is not significantly different in these locations, but because of the low dip angle,  $M_{zz}$  contributes more significantly to  $\sigma_n^M$  than to  $\tau_d^M$ , which is then dominated by horizontal compression, leading to reverse-sense shear. The stresses caused by the Pengguan massif locally resolve as right-lateral on these segments as well. Coseismic slip on these fault patches is much lower than on the steeper Beichuan fault, where the majority of slip occurred and which is topographically loaded in the opposite shear sense.

Compellingly, similar patterns exist in the spatial distributions of  $\sigma_n^M$  and coseismic slip. Most obvious is the coincidence of locally high  $\sigma_n^M$  and locally low slip magnitude on the southwestern Beichuan fault below the culmination of the Pengguan massif, in an area of otherwise high slip (Figure 4). These correlations exist for other fault patches, but they are not as clear (Figure 5). This raises the possibility that topographic loading of these faults contributes to limiting coseismic slip once failure has occurred, and may have implications for estimations of dynamic friction and the completeness of stress drop during the earthquake. Preliminary analysis of this is currently being performed, and will be described in a forthcoming manuscript.

#### 4. Calculations of tectonic stress, fault friction and pore fluid pressure

Faults fail in earthquakes when the shear stresses on the fault overcome the frictional stresses resisting slip on the

fault [e.g., Scholz, 2002]. We assume that the entire fault was at the point of failure when the Wenchuan fault initiated, and use the Mohr-Coulomb failure criterion

$$\tau = \mu(\sigma_n - \sigma_p), \quad (7)$$

where  $\mu$  is the coefficient of static friction on the fault and  $\sigma_p$  is the pore fluid pressure [e.g., Sibson, 1985]. We describe the pore fluid pressure using a scalar,  $0 \leq \phi \leq 1$ , which is the pore fluid pressure as a fraction of total pressure, and so the failure criterion is

$$\tau = \mu(1 - \phi)\sigma_n \quad (8)$$

[e.g., Sibson, 1985]. We assume that both  $\mu$  and  $\phi$  are constant across the Wenchuan faults.

We estimate the tectonic stress tensor field,  $\mu$ , and  $\phi$  consistent with published coseismic slip models of the Wenchuan earthquake using a Bayesian estimation, resulting in posterior probability density functions of the model parameters. We first estimate posteriors of  $T$  consistent with the coseismic slip models, and then estimate  $\mu$  and  $\phi$  consistent with Mohr-Coulomb failure. The nature of Bayesian estimation allows us to quantify both the relative likelihoods of model parameters and the tradeoffs between them.

#### 4.1. Description of the stress state

We consider the complete stress tensor,  $S$ , at a point in the crust to be

$$S = M + T + L, \quad (9)$$

where  $M$  is described above,  $T$  is the tectonic stress tensor, and  $L$  is the lithostatic stress tensor.  $L$  is isotropic, with diagonal components equal to  $\rho g z$ . We assume that  $T$  is latterly homogeneous and only has horizontal stress components (i.e.,  $T_{xz} = T_{yz} = T_{zz} = 0$ , with  $T_{xx}$ ,  $T_{yy}$  and  $T_{xy}$  non-zero). We further assume that  $T$  increases linearly with depth so that the entire upper crust is near the critical failure envelope [e.g., Townend and Zoback, 2000], are thus we parameterize the components of  $T$  as scalars multiplied by lithostatic pressure, denoted as  $T'$

#### 4.2. Bayesian inversion of tectonic stresses

We invert topographic stresses and coseismic slip models for tectonic stresses using Bayesian methods, and making the common ‘Wallace-Bott’ assumption (named after Wallace [1951] and Bott [1959]) that slip on the fault occurs in the general direction of the maximum resolved shear stress on the fault [e.g., McKenzie, 1969; Angelier, 1994]. We estimate the tectonic stresses in light of the topographic stresses and slip distributions through the relation

$$p(T|D) \propto p(T) p(D|T), \quad (10)$$

where  $p(T)$  is the prior PDF (or *priors*) of  $T$ ,  $p(D|T)$  is the likelihood of observing the coseismic slip distribution  $D$  given the tectonic stresses  $T$ , and  $p(T|D)$  is the posterior PDF of  $T$  given  $D$ , which is the solution to the inver-

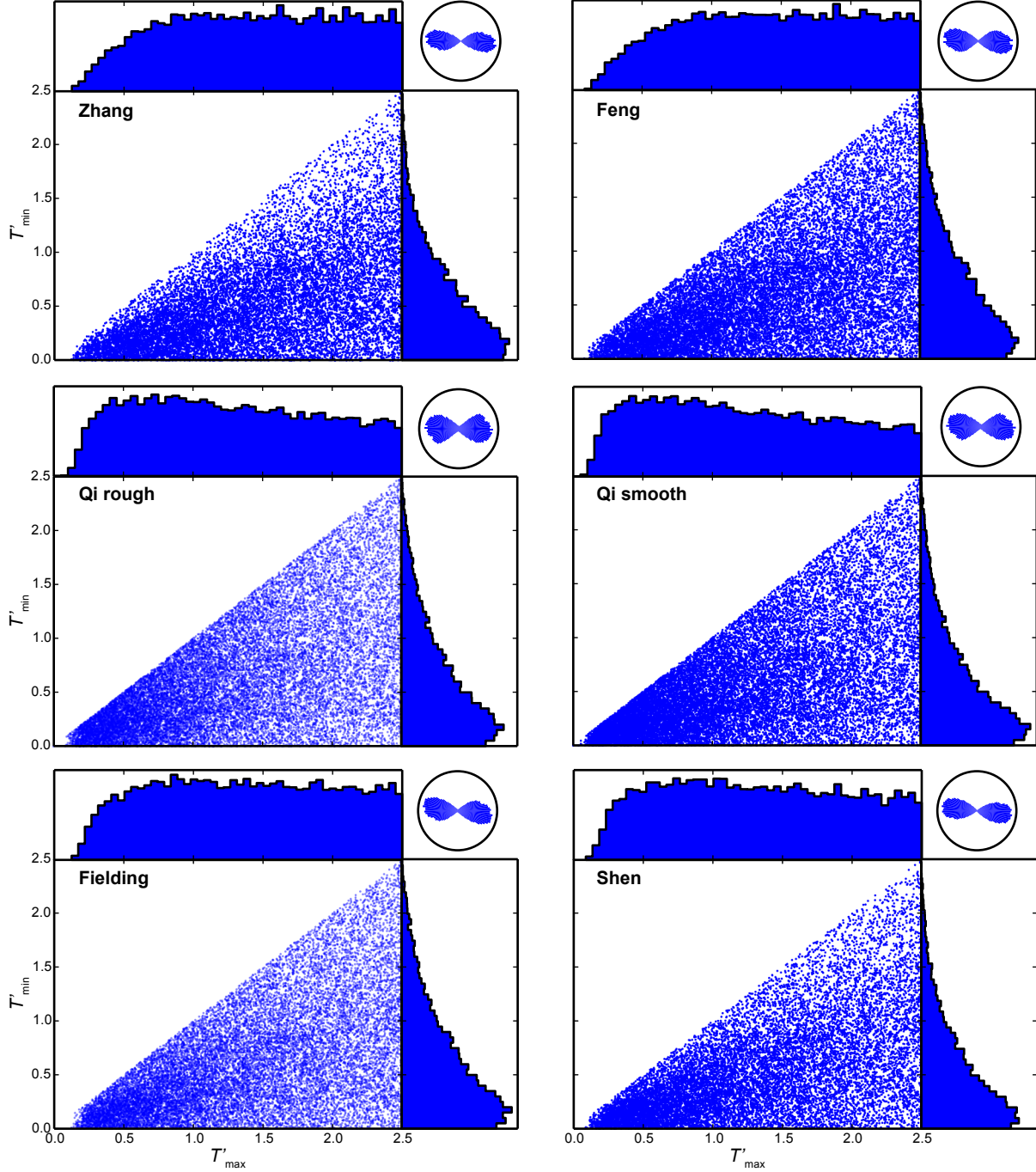


**Figure 6.** Samples of  $p(T'_\text{max}, T'_\text{min} | D)$  associated with each of the coseismic slip models we consider, along with marginals of  $T'_\text{max}$  and  $T'_\text{min}$ . Inset rose diagrams are histograms of azimuth of  $T'_\text{max}$ .

sion [e.g., Mosegaard and Tarantola, 1995]. Due to the unknown proportionality in equation (10), our posterior only gives likelihood of  $T$  relative to the most likely estimate (MLE) [Tarantola, 2005]. We follow a Monte-Carlo strategy, where samples of the prior PDF are retained as samples

of the posterior in proportion to  $p(D|T)$  [e.g., Mosegaard and Tarantola, 1995].

We parameterize  $T$  by the magnitudes and orientation of the maximum and minimum principal tectonic stresses. We assume priors such that the magnitudes of principal tectonic stresses are equally likely within bounds and that all ori-

tations are equally likely. Because the Wenchuan event was an oblique reverse faulting earthquake, we assume that total horizontal stresses are greater than the vertical stress, which is satisfied if the tectonic stresses are positive. Prior samples of maximum principal stress are taken from a uniform distribution between  $\rho_{gz}$  and  $2.5 \rho_{gz}$ . Samples of the minimum principal stress are from a uniform distribution between 0 and the value for maximum stress. We describe the orientation of the tectonic stress using the azimuth of the maximum tectonic stress, which are sampled uniformly from 0 to  $360^\circ$ .

We test 100,000 unique samples drawn from the prior using a seeded pseudorandom number generator. We test the same prior samples against each of the coseismic slip models.  $S$  is then constructed for each point discretizing the fault geometries in the coseismic slip models. The rake of the maximum shear stress  $\lambda^S$  on each point of the fault is calculated and compared to the coseismic slip rake  $\lambda^D$  at that point. A weighted mean misfit is calculated by

$$\bar{\lambda}^m = \sum_{i=1}^n \frac{(\lambda_i^S - \lambda_i^D)D_i}{\bar{D}}, \quad (11)$$

where  $D$  is the coseismic slip and  $\bar{D}$  is the average coseismic slip in a given coseismic slip model. Finally, the relative likelihood of each model is computed using a Von Mises distribution as

$$p(D|T) = \frac{\exp(\kappa \cos \bar{\lambda}^m)}{\exp(\kappa \cos \bar{\lambda}_{\min}^m)}, \quad (12)$$

where  $\kappa = 8.529$ , which is calculated so that the 68.2% confidence interval the Von Mises distribution is within  $\pi/9$  radians ( $20^\circ$ ), the estimated  $1\sigma$  uncertainty of the coseismic slip models based on comparisons between rakes of high-slip fault patches (note that for a planar fault,  $\tau$  at  $\pi/9$  radians from  $\lambda_{\max}$  is still  $>90\%$  of  $\tau_{\max}$  [Lisle, 2013]). Prior samples are retained in proportion to  $p(D|T)$ , and the retained samples are then samples of the posterior.

#### 4.3. Analysis of friction and pore fluid pressure

Once the tectonic stress distributions consistent with the coseismic slip models have been determined, we deduce the distributions of  $\mu$  and  $\phi$  assuming that the stress is at the failure criterion in equation (8). We do this in three steps: First, we draw a random  $\phi$  from a uniform distribution, assuming  $0 \leq \phi < 1$ . We again use a seeded pseudorandom number generator, such that each stress model has a uniquely assigned  $\phi$  that is consistent priors across all coseismic slip

models. Second, we calculate  $\tau^S$  and  $\sigma_n^S(1 - \phi)$  for each point on the fault. Third, we solve Equation 8 for  $\mu$ . Finally, we filter the results so that only models with  $0 \leq \mu < 1$  are retained, as values outside of that range have not been suggested for rocks.

After this analysis has been done for all coseismic slip model, we find the joint posterior (i.e., the posterior consistent with all of the coseismic slip models) by taking the samples that are common to all of the individual posteriors. We denote the joint posterior as  $p_J(P|D)$ , where  $P$  is the parameter of interest.

## 5. $T$ , $\mu$ , $\phi$ results

### 5.1. Individual slip models

Results for  $T'$ ,  $\mu$  and  $\phi$  are quite consistent across all coseismic slip models (Figure 6). Maximum compressive stress  $T'_{\max}$  is broadly east-west for all models, with a mode trending at  $90^\circ$ – $105^\circ$ .  $p(T'_{\max}|D)$  for each slip model increases from  $T' = 0$  to 0.5 or 1 before essentially leveling off, though some slip models, particularly the Qi *et al.* [2011] model, show a slight decrease in relative likelihood past the initial mode at  $T' = 0.5$ –1. The low likelihood below  $T' \approx 0.5$  indicates that lower tectonic stresses are unlikely to overcome fault friction and topographic shear stresses resisting reverse-dextral slip on the Wenchuan faults.  $p(T'_{\min}|D)$  for each slip model has a mode close to  $T'_{\min} = 0.2$  and decreases abruptly at higher values, though all slip models show values for  $T'_{\min}$  up to 2.5.  $T'_{\min}$  is typically 0–0.4 of  $T'_{\max}$ , but rarely higher.

All slip models show  $p(\phi|D)$  to be uniformly high from  $\phi = 0$  to 0.4–0.6 and to decrease linearly to  $p(\phi) = 0$  at  $\phi = 1$  (Figure 7).  $p(\mu|D)$  for all slip models has a mode at  $\mu = 0.1$ –0.4 and  $p(\mu)$  decreases at higher values.  $T'_{\max}$ ,  $\phi$  and  $\mu$  are highly correlated, where higher values of  $T'_{\max}$  are associated with higher  $\mu$  and lower  $\phi$ . Combinations of high  $\mu$  and low  $\phi$  require much higher  $T'_{\max}$  to overcome fault friction and cause slip, and so are not represented in the posteriors. Since our maximum  $T_{\max}$  of  $2.5\rho_{gz}$  is quite high ( $\approx 660$  MPa at 10 km), we view high  $\mu$  and low  $\phi$  combinations as unrealistic for the Wenchuan faults. Similarly, combinations of very low  $\mu$  and very high  $\phi$  are associated with very low  $T'_{\max}$ , and have a low probability density, as it is unlikely that tectonic stress with very low  $T'_{\max}$  values can overcome sinistral and normal-sense topographic shear stresses to cause the observed coseismic slip kinematics.

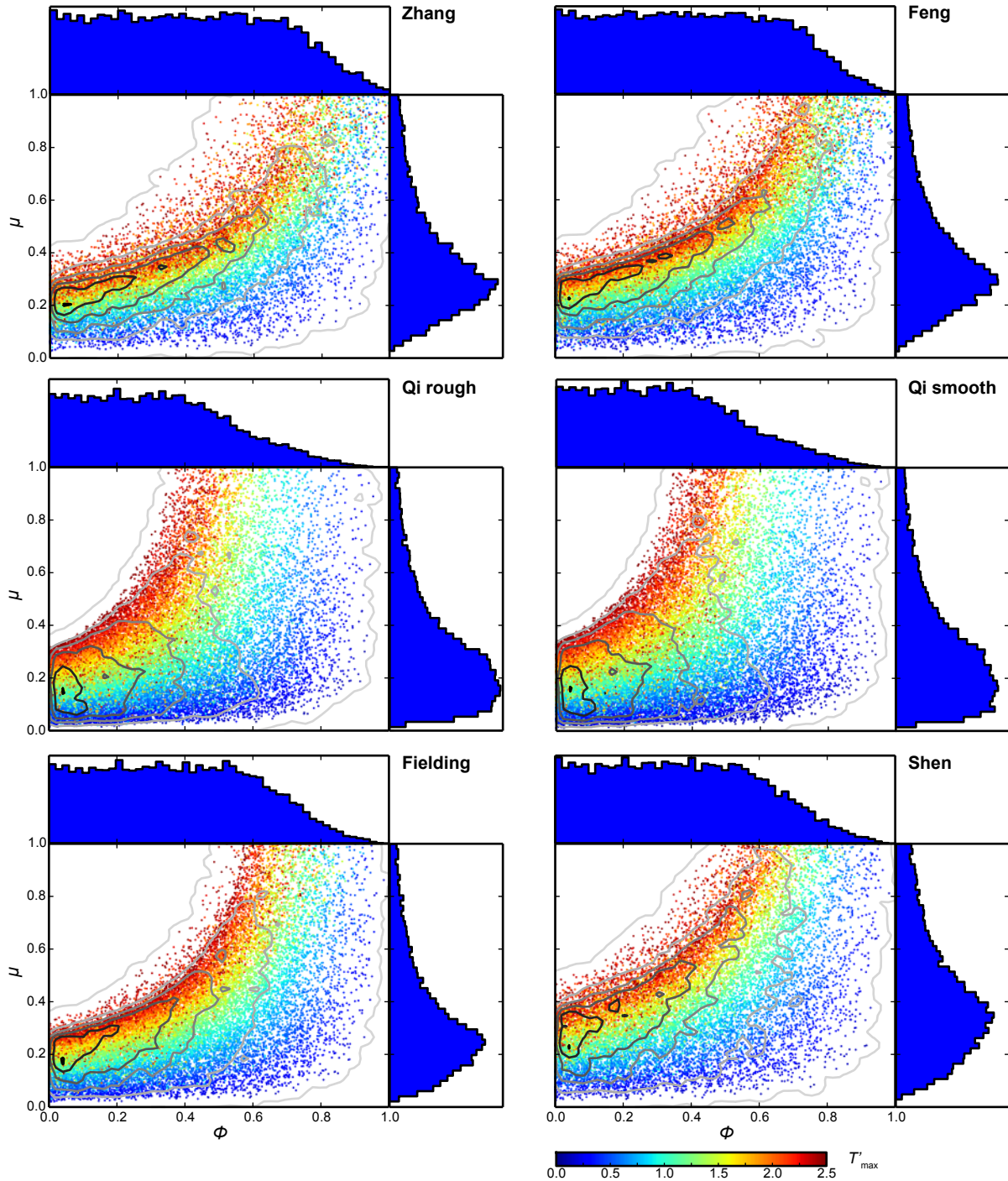


**Figure 7.** Samples of  $p(\mu, \phi | D)$  for each coseismic slip model. Colors indicate magnitude of  $T'_{\text{max}}$ . Contour lines indicate relative density (i.e., likelihood) of posteriors (darker lines signify higher densities).

## 5.2. Joint posteriors

We define a joint posterior,  $p_J(T'|D)$ , by the samples that are common to the individual posteriors estimated from each slip model. Unsurprisingly, given the broad similarity between the posteriors from the various slip models,  $p_J(T'_{\max}|D)$  is not substantially different from any of the constituent model posteriors.  $p_J(T'_{\max}|D)$  has a somewhat more well-defined mode at  $T'_{\max} \approx 0.6$ .

In our estimation of  $\phi$  and  $\mu$  in the posteriors associated with each slip model, we have used the same random combinations of  $T$  and  $\phi$  for each slip model, and then solved for  $\mu$  so that the fault is at a critical stress state (Equation 8). Because of differences in the location and slip among the coseismic slip models, some variability exists in  $\mu$  for each prior sample. We therefore choose  $p_J(\mu|D)$  to be the median  $\mu$  of each slip model for each sample.  $p_J(\mu|D)$  has a mostly similar distribution as  $p(\mu|D)$  for any of the slip models. However,  $p_J(\mu|D)$  has a lower relative likelihood on the high- $\mu$  tail compared to the constituent  $p(\mu|D)$ . This lower likelihood of  $\mu$  in the joint posterior is likely because it is the average  $\mu$  of all slip models. On the other hand, it is not similarly sparse on the low- $\mu$  side, suggesting that low values for  $\mu$  are more robust.

## 6. Discussion

Few studies have performed similar quantification of static stress fields on faults (see Section 1.1 for some examples), even though it may have important ramifications to the earthquake process. Most studies of fault rupture dynamics assume either a homogeneous or stochastic shear stress distribution [e.g., Oglesby and Day, 2002] and few assume any variation in normal stress [e.g., Agaard *et al.*, 2001], despite the importance that stress variations likely have in earthquake dynamics [e.g., Day, 1982; Olsen *et al.*, 1997]. Additionally, quantifying friction and pore fluid pressure involved in faulting is a major challenge in studies of faulting and orogenic dynamics [e.g., Meissner and Strehlau, 1982; Oglesby and Day, 2002].

Previous workers have demonstrated that by quantifying topographic stress, other components in the Coulomb stress balance may be bracketed [e.g., Cattin *et al.*, 1997; Lamb, 2006; Luttrell *et al.*, 2011]. Each of these studies uses somewhat different approaches. Our approach is most similar to that of Luttrell *et al.* [2011], although there are significant differences: (1) We use the topographic stress calculations proposed by Liu and Zoback [1992], whereas Luttrell *et al.* [2011] only uses the vertical loading from topography, equivalent to  $M^B$  in equation (3). (2) We do not consider buoyancy forces due to lateral variations in density, due for instance to Moho variation, as done by Luttrell *et al.* [2011]. In the Longmen Shan region, Moho variation is small compared to the change in Moho depths at the Andean plate boundary, and so the buoyancy terms should be relatively small. (3) We consider a full range of tectonic stresses, in-

stead of simply calculating the minimum principal tectonic stress and its orientation. (4) We consider the stress tensor at each point due to topographic loading, lithostatic stress, and horizontal tectonic stress, and use inferred coseismic slip rake as a constraint on the allowable stresses, rather than inferring the earthquake stress drop from the coseismic slip models, as done by Luttrell *et al.* [2011]. (5) We use both normal and shear stresses to constrain pore fluid pressure and friction. (6) We use a Bayesian estimation, resulting in a PDF of tectonic stress, as well as  $\mu$  and  $\phi$ , rather than just solving for the minimum tectonic stress required for faulting, as done by Luttrell *et al.* [2011].

### 6.1. Topographic stresses on the Wenchuan faults

Topographic stresses on the main Wenchuan faults are of considerable magnitude:  $\tau^M$  ranges from about -20 to 10 MPa, which is on the order of inferred stress drop in earthquakes [e.g., Kanamori and Anderson, 1975; Allmann and Shearer, 2009]. Topographic stresses are generally opposed to the tectonic slip direction, and therefore have to be overcome by tectonic stresses in order to produce the observed rupture patterns. The topographic shear stresses are likely persistent over the lifespan of the topography (i.e. on the order of millions to tens of millions of years), otherwise the Wenchuan faults may fail in a normal sense simply due to the weight of the Longmen Shan. This would argue that tectonic stress drop in the Wenchuan earthquake was not complete, as some residual tectonic shear stress must remain on the fault to cancel out  $\tau^M$ .

The spatial variation of topographic stresses decreases in frequency and amplitude with depth. This is not surprising, because with increasing depth, the stress field at any point is more sensitive to surface loads averaged over a greater region, and is less dominated by smaller scale topographic features (i.e., individual mountains). The spatial variability of the topographic stress with depth is similar to the spatial variability of coseismic slip in the models considered [e.g., Zhang *et al.*, 2011], which are both smoother at depth. Some of the estimated slip variability is likely partially due to the more limited resolution of coseismic slip at depth using geodetic data. However, the negative spatial correlations of slip versus stress (especially  $\sigma_n^M$ ) (Figures 4, 5) suggest this may be a real signal.

### 6.2. Tectonic stresses in eastern Tibet

The maximum tectonic stress,  $T_{\max}$ , is consistently oriented roughly E-W in our results. This orientation is oblique to the Longmen Shan, which produces oblique (right-lateral and reverse sense) shear on the Beichuan fault.  $T_{\min}$  is ~N-S oriented, and is only slightly larger than lithostatic pressure. This stress configuration is compatible with the observed kinematics of the Wenchuan faults, and in close agreement pre-earthquake stress measurements near the rupture zone (Figure 9), mostly from borehole breakout data from 2-5 km depth [Heidbach *et al.*, 2009], which is the zone of maximum slip in the coseismic slip models. It is somewhat discrepant with stress orientations estimated at ~800 m depth

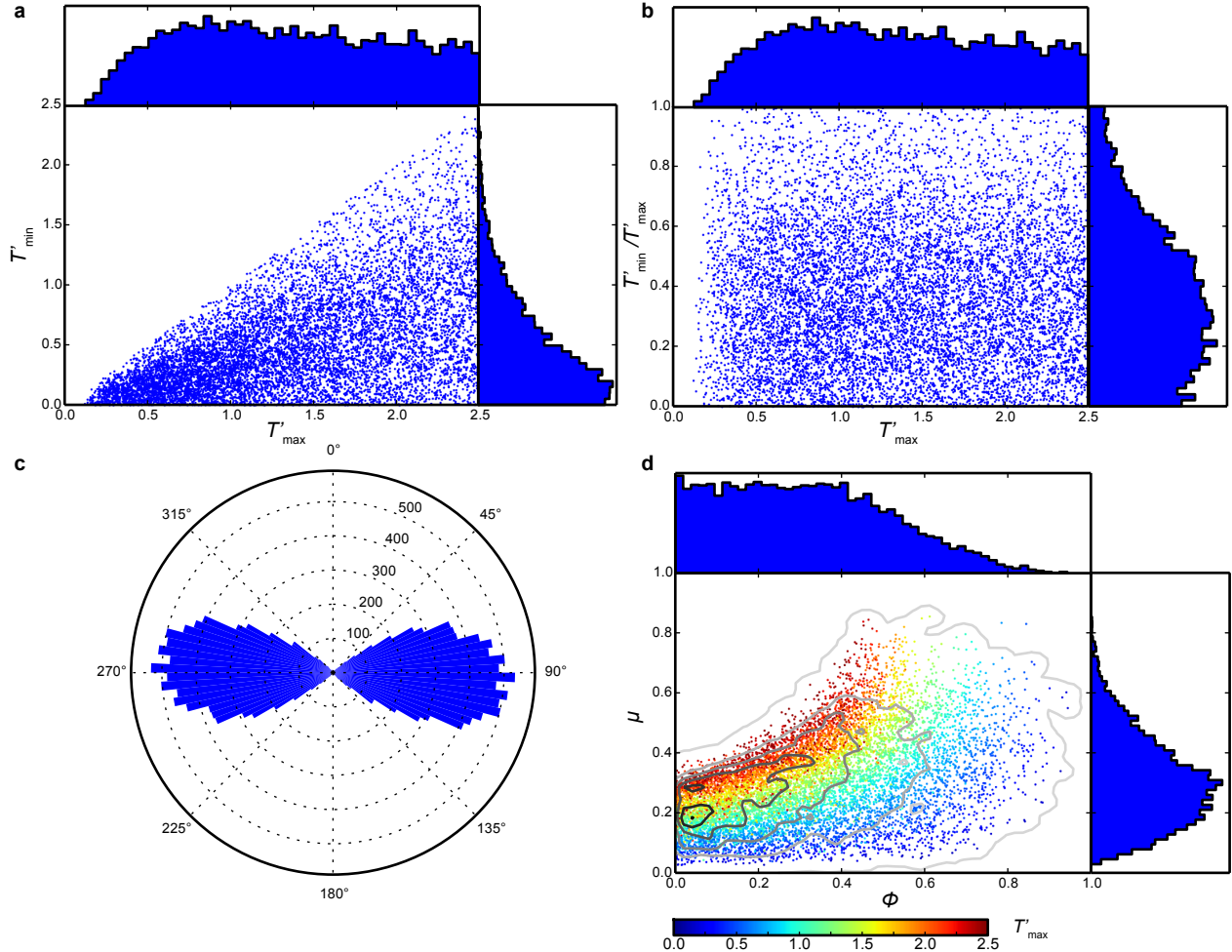


**Figure 8.** (a) Samples of  $p_J(T'_{\max}, T'_{\min}|D)$ , along with marginals of  $T'_{\max}$  and  $T'_{\min}$ . (b) Samples of  $p_J(T'_{\max}, T'_{\min}/T'_{\max}|D)$ , along with marginals of  $T'_{\max}$  and  $T'_{\min}/T'_{\max}$ . (c) Histogram of azimuths of  $T'_{\max}$ . (d) Samples of  $p_J(\mu, \phi|D)$ , with marginals, where color of the samples indicate magnitudes of  $T'_{\max}$  and contour lines indicate relative density (i.e., likelihood of posteriors (darker lines signify higher densities).

adjacent to the Beichuan fault in the WFSD-1 borehole of the Wenchuan Earthquake Fault Scientific Drilling Project several years after the 2008 earthquake [Cui *et al.*, 2014], which show  $\sigma_{H\max}$  to be more orthogonal to the fault trace, suggesting that much of the right-lateral component of shear stress was released during the earthquake. These results are similar to the orientations of total stress obtained by *Medina Luna and Hetland* [2013], although they were unable to constrain the magnitudes of stresses.

The magnitudes of  $T_{\max}$  and  $T_{\min}$  are dominantly constrained on the low end by our analysis, which is apparent by the sharp decrease in the frequency of  $p(T_{\max}|D)$  below about  $T' = 0.5$ . This indicates that  $T_{\max}$  of at least  $\sim 13.25$  MPa km $^{-1}$  is necessary to overcome topographic stresses resisting reverse and right-lateral slip on the faults. We find that the highest likely ratio of strike-slip to dip-slip shear along the Wenchuan earthquake faults is close to 1. This is similar to the inferences of strain accumulation rates inferred from squishy block modeling by Loveless and Meade [Loveless and Meade, 2011], who concluded that the rate of

slip deficit accumulation in the thrust and dextral sense was approximately equal. It should be noted that the tectonic stresses we estimate here represent the accumulated stresses prior to the Wenchuan earthquake, and the relation of these stresses to accumulated slip deficit needs to be through a model of strain accumulation.

The orientation of both the tectonic and total stresses near the Wenchuan faults shows a larger difference with patterns of strain from elsewhere in the orogen. For example, the presence of N-S contraction and E-W extension throughout the high Tibetan plateau and much of the Himalaya [e.g., Armijo *et al.*, 1986; Molnar and Lyon-Caen, 1988; Taylor *et al.*, 2003] indicates a roughly N-S  $T_{\max}$  and E-W  $T_{\min}$ . Because  $T_{\min}$  is only slightly above lithostatic pressure on the Wenchuan faults, it is quite possible that the N-S compression in the Himalaya and Tibet, which is almost certainly due to Indo-Asian plate collision, has significantly decayed at the Longmen Shan, some 850 km northeast of the easternmost Himalaya. Therefore, contraction across the Longmen Shan cannot easily be interpreted to directly reflect stresses

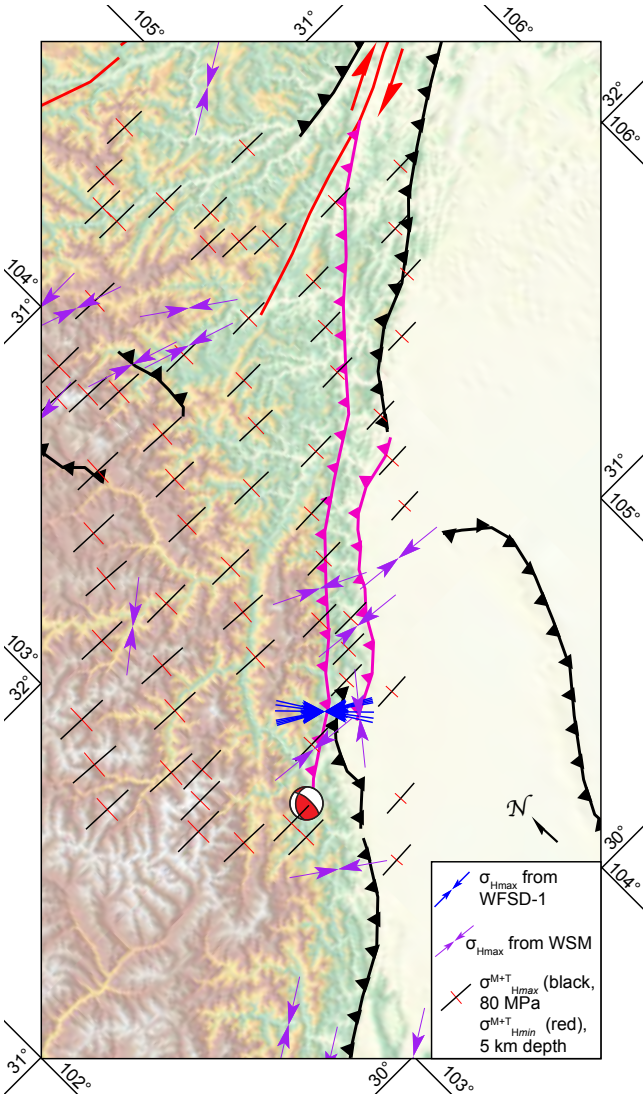


**Figure 9.** Topographic and tectonic horizontal stresses (taken from the most likely estimates of  $p(T|D)$  in the Wenchuan rupture region (black and red crosses) with horizontal maximum stress orientation data taken from before the 2008 Wenchuan event from the World Stress Map [Heidbach *et al.*, 2009] (purple arrows), and horizontal maximum stress orientation data from after the earthquake at the WFSD-1 drill hole [Cui *et al.*, 2014] (blue arrows). Other symbols are as in Figure 1. Stresses shown are downsampled from our computational grid resolution by a factor of nine.

due to the Indo-Asian collision alone, unless some additional mechanism of redirecting crustal stresses is incorporated.

### 6.3. Slip on the Beichuan fault vs. optimally-oriented faults

Our highest likelihood estimates of  $\mu$  are in the range of 0.2–0.3. These values are slightly lower than  $\mu \approx 0.4$  inferred in laboratory experiments on samples recovered from the WFSD-1 drill hole into the Beichuan fault [Kuo *et al.*, 2014]. However, it should be noted that  $\mu \approx 0.4$  is relatively high likelihood in our posteriors (Figure 8). These values of friction are lower than typical values derived from labor-

atory experiments on intact rock [e.g., Byerlee, 1978], suggesting that slip occurred on preexisting faults because they are weaker than optimally-oriented new faults.

The obliquity of slip on the Wenchuan earthquake faults also suggests that these faults may not be optimally oriented for slip given the total stress state in the region of these faults. However, the Longmen Shan fault zone dates back to the Indosinian orogeny, locally late Triassic (226–206 Ma) [Yong *et al.*, 2003] and has had multiple episodes of reactivation since [e.g., Burchfiel *et al.*, 1995; Wang *et al.*, 2012], accumulating tens of kilometers of shortening [e.g., Hubbard *et al.*, 2010]. Such a mature fault system may be expected to have low coefficients of friction due to processes such as gouge development [e.g., Kuo *et al.*, 2014], and therefore may slip in non-optimal orientations, with high  $\phi$  values also potentially contributing to this [e.g., Sibson, 1985].

Our posterior estimates for  $T$ ,  $\phi$  and  $\mu$  let us quantitatively evaluate to what extent slip on the Wenchuan faults is

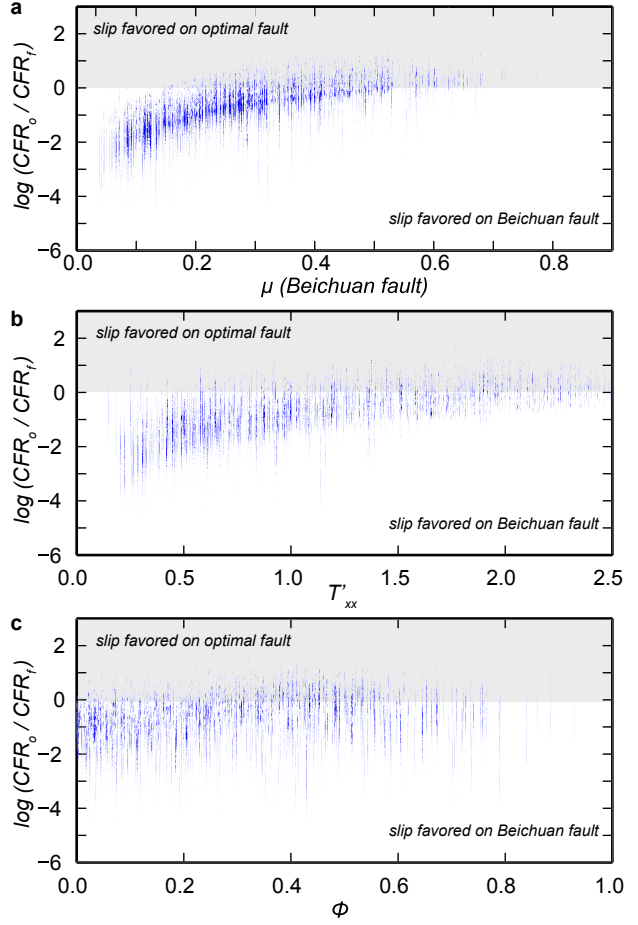


**Figure 10.** Comparison of Coulomb failure ratio (CFR) on the Beichuan fault from the Zhang *et al.* [2011] coseismic slip model to CFR on an optimally-oriented fault with  $\mu = 0.6$ , versus estimated  $\mu$  on the Beichuan fault. Values less than 0 (1 in linear space) indicate that slip is favored on the Beichuan fault, even if it is not optimally oriented. Values are calculated for each point in the slip model for 1000 randomly-drawn samples from  $p(T, \mu, \phi | D)$ .

more favorable than on optimally oriented faults with more typical friction coefficients. We use the same failure conditions as in determining the posteriors above, and assume optimally oriented faults exist (i.e., we do not consider the generation of new faults in relatively intact rock). Additionally, we evaluate the relative contributions of  $T$ ,  $\phi$  and  $\mu$  on potential fault weakening and reactivation. To explore these relationships, we perform some preliminary analysis on a single fault model (from *Zhang et al.* [2011]) using a subset of 1000 samples drawn randomly from the joint posteriors. Given the similarity of the fault models and of the posteriors for each model, we do not expect that an analysis of all results on all fault models will yield different conclusions.

First, we establish a metric with which to evaluate the favorability of slip on a given fault plane, which we call the Coulomb failure ratio, or CFR:

$$\text{CFR} = \tau/\mu(1-\phi)\sigma_n . \quad (13)$$

CFR indicates whether a fault should fail under a given stress state:  $\text{CFR} > 1$  indicates failure, while a  $\text{CFR} < 1$  indicates fault stability. We then calculate the CFR on each point in the model of the Beichuan fault (594 points describe the fault model of *Zhang et al.* [2011]) based on the full stress field  $S$  at each point on the fault, for each of the 1000 samples of  $T$ ,  $\phi$  and  $\mu$  drawn randomly from the posteriors. We call this  $\text{CFR}_f$ . Then, using the same  $S$  and  $\phi$ , we calculate the CFR on an optimally oriented fault with  $\mu = 0.6$  and no cohesion, which we call  $\text{CFR}_o$ . Note this  $\mu$  is typical for crustal rocks with fault normal stresses above 200 MPa, but lower than  $\mu = 0.85$  for smaller  $\sigma_n$  [*Byerlee*, 1978], but may be appropriate for an immature crustal fault.

Figure 10 shows  $\log(\text{CFR}_o/\text{CFR}_f)$  plotted against  $\mu$ ,  $\phi$  and  $T'_{xx}$  on the Beichuan fault for all samples. Though considerable scatter exists, it is clear that in most instances, slip on the Beichuan fault is preferred over slip on an optimal fault. The exceptions are at high values of  $\mu$ ,  $\phi$ , or  $T'$ , where slip on an optimal plane is preferred. Because  $T$ ,  $\phi$  and  $\mu$  can all affect fault reactivation [e.g., *Sibson*, 1985], we compare the relative contributions of each with a simple multiple linear regression, using  $T'_{xx}$  normalized to [0,1] (the same range  $\phi$  and  $\mu$ ) as a proxy for  $T$  ( $T'_{xx}$  is essentially  $T'_{\max}$  in most of the posteriors). The results are shown in Table 2. It is clear that  $\mu$  is most strongly correlated with  $\text{CFR}_o/\text{CFR}_f$ , followed closely by  $T'_{xx}$  and then  $\phi$ ; nonetheless, all significantly affect the relative ease of faulting on the Beichuan fault versus optimal faults.

**Table 2.** Sensitivity of CFR ratios to relevant stress state parameters: Results of multivariate linear regression of  $\text{CFR}_o/\text{CFR}_f$  against  $\mu$ ,  $\phi$  and  $T'_{xx}$ .

Parameter	Coef.	Std. Err.	t statistic	$P >  t $
Intercept	-0.2566	0.0020	-128.8	<0.0001
$\mu$	1.1168	0.0086	130.6	<0.0001
$T'_{xx}$	0.9138	0.0048	191.2	<0.0001
$\phi$	0.5762	0.0055	105.7	<0.0001

#### 6.4. The role of topography in orogenic development and strain localization

Because the rise of broad elevated regions creates significant stresses in the crust [e.g., *Jeffreys*, 1924], these stresses have the potential to influence orogenesis. The result may be to change the deformation state in the interior of the orogen [e.g., *Dewey*, 1988; *Molnar and Lyon-Caen*, 1988], the convergence rates of the plates surrounding the orogen [e.g. *Meade and Conrad*, 2008], or the location and style of deformation at the orogen's margins [e.g., *Beaumont et al.*, 2001; *DeCelles et al.*, 2009]. These studies show that as an orogen rises, horizontal contraction via crustal thickening will occur at the thin margins of the orogen, and if elevations reach a threshold or tectonic compression decreases, extension will take place in the orogen's high interior, as is well described in Tibet. Therefore, Tibet is commonly suggested to be undergoing some manner of gravitational collapse [e.g., *England and Houseman*, 1989]; where the plateau abuts rigid cratons, the deformational patterns resemble 'fixed boundary' collapse [*Rey et al.*, 2001], with concentrated crustal thickening at the orogen's margins [e.g., *Cook and Royden*, 2008].

Though much work has been done exploring the feedback mechanisms between topography and deformation; however, topography is typically greatly smoothed, and topographic stresses are folded into gravitational potential energy estimates of the entire lithosphere, and the whole lithospheric column is often considered viscous [*Copley and McKenzie*, 2007]. Therefore many models seeking to predict deformation from gravitational forces yield continuous deformation and do not consider how the gravitational stresses resolve on heterogeneities embedded in the crust. However, the presence of structures such as weak faults [*Bird and Kong*, 1994] or low-viscosity channels or shear zones [e.g., *Clark et al.*, 2005] can localize deformation [e.g., *Bird and Kong*, 1994; *Flesch and Bendick*, 2012].

Our results that topographic stresses on the Wenchuan earthquake faults are largely loaded in the opposite sense to the coseismic slip direction indicates that gravitational collapse is probably not the driver of reverse faulting in the Longmen Shan. However, as noted previously, thrust flats in the middle crust present in some coseismic slip models, particularly the Qi model, are loaded in a thrust and dextral sense. Given the very low dips of the thrust flats ( $0^\circ$ – $5^\circ$ ), they receive very little loading from horizontal tectonic stress, so any slip on them may be in response to topographic loading and thus to gravitational collapse of the high Longmen Shan and its hinterland.  $M_{H\max}$  also changes orientation

tion from fault rangefront normal to closer to more oblique near the front of the range (Figure 3), suggesting that any transfer of mass from the highlands to the lowlands due to topographic stresses should terminate near the rangefront.

However, because  $M_{zz}$  is greater than  $M_{H\max}$  underneath the higher topography, topographic stresses can only lead to reverse faulting on the Wenchuan faults if subhorizontal shear zones or channels are present, and are very weak so shear can occur at low  $\tau$  relative to  $\sigma_n$ . This conclusion has been reached in studies of generalized orogens [e.g., Flesch and Bendick, 2012] and gravitational collapse of volcanic edifices [e.g., Byrne *et al.*, 2013], indicating that is a general requirement of gravitational spreading. Our calculations of  $\mu$  and  $\phi$  are based on  $T$ , which is biased towards the high slip patches in the upper crust (Equation 5), yield low  $\mu$  and low to moderate  $\phi$ , which is probably insufficient for slip at high pressures at depth. Similarly, a low viscosity horizontal channel that underlies eastern Tibet, likely much deeper than the seismogenic zone we consider here, would be able to flow in response to  $\tau$  regardless of  $\sigma_n$  and may be able to facilitate gravitational spreading of the orogen [e.g., Clark *et al.*, 2005; Cook and Royden, 2008; Flesch and Bendick, 2012].

These arguments are all quite speculative, and we wish only to describe the conditions under which gravitational collapse can occur given the observations of deformation and the topographic stress field. It is not at all clear that a suitably large decollement exists at the base of the Beichuan fault (it is only present in one of the slip models considered). Nonetheless, this topic has implications not only for orogenic development, but for the recurrence interval on the Wenchuan earthquake faults. If topographic stress contributes in some fashion to the observed displacements on the fault, then those stresses were likely barely diminished by coseismic stress change, and earthquake recurrence on the Wenchuan faults may be governed by different processes than elastic rebound due to tectonic strain accumulation.

## 7. Conclusions

We have calculated shear and normal stresses due to topographic loading on the Wenchuan earthquake faults, and used those stresses to constrain tectonic stresses, fault friction and pore fluid pressure. Topographic stresses on the main Wenchuan faults are large, with  $\tau^M$  on the faults up to |20| MPa, and  $\sigma_n^M$  up to 80 MPa.  $\sigma_n^M$  reaches up to 100 MPa on mid-crustal thrust flats present in some coseismic slip models. The direction of  $\tau_M$  is generally opposed to coseismic slip inferred during the 2008 Wenchuan earthquake, indicating that weight of the topography resists coseismic slip. High values of  $\sigma_n^M$  increase the frictional resistance to slip, potentially limiting slip magnitude in locations such as below the Pengguan massif.

Assuming that the Beichuan faults were at a Mohr-Coulomb fault criterion immediately prior to the Wenchuan earthquake, we estimate the tectonic stresses required for the faults to fail. We use a Bayesian estimation, resulting in posteriors representing likelihood of tectonic stress, static fric-

tion, and a pore pressure parameter. The posteriors indicate that the maximum tectonic stress is oriented ~E-W and has a likely minimum of 13.25 MPa km<sup>-1</sup>. The minimum tectonic stress is oriented ~N-S and is fairly low, with highest likelihood one half of the E-W tectonic stress. The highest likelihood coefficient of static friction on the fault is estimated at about 0.2–0.3, although values up to 0.5–0.6 are permissible. Fluid pressures are likely 0–0.5 of the total pressure.

Slip occurred on these faults instead of more favorably-oriented faults elsewhere in the region, due to the inferred low coefficient of friction and moderate fluid pressures.

## Appendix A: Green's functions for point-source loads

For completeness, we reproduce the Boussinesq [e.g., Jeffreys, 1970] and Cerruti [e.g., Love, 1927] solutions here. Note that in these solutions,  $\lambda$  and  $\mu$  are re-defined, and are the first and second Lame's parameters, respectively, instead of rake and fault friction as in the body of the manuscript.

### A1. Boussinesq's solutions for vertical point-source loads

$$G_{xx}^B = \frac{F_v}{2\pi} \left[ \frac{3x^2}{r^5} + \frac{\mu(y^2+z^2)}{(\lambda+\mu)r^3(z+r)} - \frac{\mu z}{(\lambda+\mu)r^3} \right. \\ \left. - \frac{\mu x^2}{(\lambda+\mu)r^2(z+r)^2} \right] \quad (A1)$$

$$G_{yy}^B = \frac{F_v}{2\pi} \left[ \frac{3y^2}{r^5} + \frac{\mu(x^2+z^2)}{(\lambda+\mu)r^3(z+r)} - \frac{\mu z}{(\lambda+\mu)r^3} \right. \\ \left. - \frac{\mu y^2}{(\lambda+\mu)r^2(z+r)^2} \right] \quad (A2)$$

$$G_{xy}^B = \frac{F_v}{2\pi} \left[ \frac{3xyz}{r^5} - \frac{\mu xy(z+2r)}{(\lambda+\mu)r^3(z+r)^2} \right] \quad (A3)$$

$$G_{zz}^B = 3F_vz^3/2\pi r^5 \quad (A4)$$

$$G_{xz}^B = 3F_vxz^2/2\pi r^5 \quad (A5)$$

$$G_{yz}^B = 3F_vyz^2/2\pi r^5 \quad (A6)$$

### A2. Cerruti's solutions for horizontal point-source loads

$$G_{xx}^{C_x} = \frac{F_{h,x}x}{2\pi r^3} \left[ \frac{3x^2}{r^2} - \frac{\mu}{(\lambda+\mu)(z+r)^2} \right. \\ \left. (r^2-y^2-\frac{2ry^2}{r+z}) \right] \quad (A7)$$

$$G_{yy}^{C_x} = \frac{F_{h,x}x}{2\pi r^3} \left[ \frac{3y^2}{r^2} - \frac{\mu}{(\lambda+\mu)(z+r)^2} \right. \\ \left. (3r^2-x^2-\frac{2rx^2}{r+z}) \right] \quad (A8)$$

$$G_{xy}^{Cx} = \frac{F_{h,x}x}{2\pi r^3} \left[ \frac{3x^2}{r^2} - \frac{\mu}{(\lambda + \mu)(z+r)^2} \cdot (r^2 - x^2 - \frac{2rx^2}{r+z}) \right] \quad (A9)$$

$$G_{zz}^{Cx} = \frac{3F_{h,x}x z^2}{2\pi r^5} \quad (A10)$$

$$G_{xz}^{Cx} = \frac{3F_{h,x}z^2}{2\pi r^5} \quad (A11)$$

$$G_{yz}^{Cx} = \frac{3F_{h,x}xyz}{2\pi r^5} \quad (A12)$$

**Acknowledgments.** Joe Kington wrote the code to plot Figure 8c.

## References

- Aagaard, B. T., T. H. Heaton, and J. F. Hall (2001), Dynamic earthquake ruptures in the presence of lithostatic normal stresses: Implications for friction models and heat production, *Bulletin of the Seismological Society of America*, 91(6), 1765–1796.
- Allmann, B. P., and P. M. Shearer (2009), Global variations of stress drop for moderate to large earthquakes, *Journal of Geophysical Research: Solid Earth* (1978–2012), 114(B1).
- Angelier, J. (1994), Fault slip analysis and paleostress reconstruction, *Continental deformation*, 4.
- Armijo, R., P. Tappouer, J. Mercier, and T.-L. Han (1986), Quaternary extension in southern Tibet: Field observations and tectonic implications, *Journal of Geophysical Research: Solid Earth* (1978–2012), 91(B14), 13,803–13,872.
- Beaumont, C., R. A. Jamieson, M. Nguyen, and B. Lee (2001), Himalayan tectonics explained by extrusion of a low-viscosity crustal channel coupled to focused surface denudation, *Nature*, 414(6865), 738–742.
- Bird, P., and X. Kong (1994), Computer simulations of California tectonics confirm very low strength of major faults, *Geological Society of America Bulletin*, 106(2), 159–174.
- Bird, P., and K. Piper (1980), Plane-stress finite-element models of tectonic flow in southern California, *Physics of the earth and planetary interiors*, 21(2), 158–175.
- Bollinger, L., J. Avouac, R. Cattin, and M. Pandey (2004), Stress buildup in the Himalaya, *Journal of Geophysical Research: Solid Earth*, 109(B11).
- Bott, M. H. P. (1959), The mechanics of oblique slip faulting, *Geological Magazine*, 96(02), 109–117.
- Burchfiel, B., C. Zhiliang, L. Yuping, and L. Royden (1995), Tectonics of the Longmen Shan and adjacent regions, central China, *International Geology Review*, 37(8), 661–735.
- Burchfiel, B., L. Royden, R. van der Hilst, B. Hager, Z. Chen, R. King, C. Li, J. Lü, H. Yao, and E. Kirby (2008), A geological and geophysical context for the Wenchuan earthquake of 12 May 2008, Sichuan, People's Republic of China, *GSA Today*, 18(7), 4–11.
- Byerlee, J. (1978), Friction of rocks, *Pure and applied Geophysics*, 116(4–5), 615–626.
- Byrne, P., E. Holohan, M. Kervyn, B. v. W. de Vries, V. R. Troll, and J. Murray (2013), A sagging-spreading continuum of large volcano structure, *Geology*, 41(3), 339–342.
- Cattin, R., H. Lyon-Caen, and J. Chéry (1997), Quantification of interplate coupling in subduction zones and forearc topography, *Geophysical Research Letters*, 24(13), 1563–1566.
- Clark, M. K., and L. H. Royden (2000), Topographic ooze: Building the eastern margin of Tibet by lower crustal flow, *Geology*, 28(8), 703–706.
- Clark, M. K., J. W. Bush, and L. H. Royden (2005), Dynamic topography produced by lower crustal flow against rheological strength heterogeneities bordering the Tibetan Plateau, *Geophysical Journal International*, 162(2), 575–590.
- Coblenz, D. D., and R. M. Richardson (1996), Analysis of the South American intraplate stress field, *Journal of Geophysical Research: Solid Earth* (1978–2012), 101(B4), 8643–8657.
- Cook, K. L., and L. H. Royden (2008), The role of crustal strength variations in shaping orogenic plateaus, with application to Tibet, *Journal of Geophysical Research: Solid Earth* (1978–2012), 113(B8).
- Copley, A., and D. McKenzie (2007), Models of crustal flow in the India–Asia collision zone, *Geophysical Journal International*, 169(2), 683–698.
- Copley, A., F. Boait, J. Hollingsworth, J. Jackson, and D. McKenzie (2009), Subparallel thrust and normal faulting in Albania and the roles of gravitational potential energy and rheology contrasts in mountain belts, *Journal of Geophysical Research: Solid Earth*, 114(B5).
- Cui, J., W. Lin, L. Wang, L. Gao, Y. Huang, W. Wang, D. Sun, Z. Li, C. Zhou, H. Qian, et al. (2014), Determination of three-dimensional in situ stresses by anelastic strain recovery in Wenchuan Earthquake Fault Scientific Drilling Project Hole-1 (WFSD-1), *Tectonophysics*, 619620, 123–132.
- Dahlen, F. (1990), Critical taper model of fold-and-thrust belts and accretionary wedges, *Annual Review of Earth and Planetary Sciences*, 18, 55.
- Dalmayrac, B., and P. Molnar (1981), Parallel thrust and normal faulting in Peru and constraints on the state of stress, *Earth and Planetary Science Letters*, 55(3), 473–481.
- Day, S. M. (1982), Three-dimensional simulation of spontaneous rupture: The effect of nonuniform prestress, *Bulletin of the Seismological Society of America*, 72(6A), 1881–1902.
- DeCelles, P. G., M. N. Ducea, P. Kapp, and G. Zandt (2009), Cyclicity in cordilleran orogenic systems, *Nature Geoscience*, 2(4), 251–257.
- Dewey, J. F. (1988), Extensional collapse of orogens, *Tectonics*, 7(6), 1123–1139.
- England, P., and G. Houseman (1989), Extension during continental convergence, with application to the Tibetan plateau, *Journal of Geophysical Research: Solid Earth* (1978–2012), 94(B12), 17,561–17,579.
- Farr, T. G., P. A. Rosen, E. Caro, R. Crippen, R. Duren, S. Hensley, M. Kobrick, M. Paller, E. Rodriguez, L. Roth, et al. (2007), The shuttle radar topography mission, *Reviews of geophysics*, 45(2).
- Feng, G., E. A. Hetland, X. Ding, Z. Li, and L. Zhang (2010), Coseismic fault slip of the 2008 Mw 7.9 Wenchuan earthquake estimated from InSAR and GPS measurements, *Geophysical research letters*, 37(1).
- Fielding, E. J., A. Sladen, Z. Li, J.-P. Avouac, R. Bürgmann, and I. Ryder (2013), Kinematic fault slip evolution source models of the 2008 Mw 7.9 Wenchuan earthquake in China from SAR interferometry, GPS and teleseismic analysis and implications for Longmen Shan tectonics, *Geophysical Journal International*, 194(2), 1138–1166.
- Flesch, L., and R. Bendick (2012), The relationship between surface kinematics and deformation of the whole lithosphere, *Geology*, 40(8), 711–714.
- Flesch, L. M., and C. Kreemer (2010), Gravitational potential energy and regional stress and strain rate fields for continental plateaus: Examples from the central Andes and Colorado Plateau, *Tectonophysics*, 482(1), 182–192.
- Heidbach, O., M. Tingay, and A. Barth (2009), *The World Stress Map based on the database release 2008, equatorial scale 1:46,000,000*, Commission for the Geological Map of the World, Paris.
- Hubbard, J., J. H. Shaw, and Y. Klinger (2010), Structural setting of the 2008 Mw 7.9 Wenchuan, China, earthquake, *Bulletin of the Seismological Society of America*, 100(5B), 2713–2735.
- Jarvis, A., H. Reuter, A. Nelson, and E. Guevara (2008), Hole-filled SRTM for the globe version 3, available from the CGIAR-CSI SRTM 90m database, Accessed: March 12, 2012.
- Jeffreys, H. (1924), *The Earth: its origin, history and physical constitution*, Cambridge University Press.
- Jeffreys, H. (1970), *The Earth*, Cambridge University Press.
- Kanamori, H., and D. L. Anderson (1975), Theoretical basis of some empirical relations in seismology, *Bulletin of the Seismological Society of America*, 65(5), 1073–1095.
- Kuo, L.-W., H. Li, S. A. Smith, G. Di Toro, J. Suppe, S.-R. Song, S. Nielsen, H.-S. Sheu, and J. Si (2014), Gouge graphitization and dynamic fault weakening during the 2008 Mw 7.9 Wenchuan earthquake, *Geology*, 42(1), 47–50.
- Lamb, S. (2006), Shear stresses on megathrusts: Implications for mountain building behind subduction zones, *Journal of Geophysical Research: Solid Earth*, 111(B7).
- Liang, S., W. Gan, C. Shen, G. Xiao, J. Liu, W. Chen, X. Ding, and D. Zhou (2013), Three-dimensional velocity field of present-day crustal motion of the Tibetan Plateau derived from GPS measurements, *Journal of Geophysical Research: Solid Earth*, 118(10), 5722–5732.
- Lin, A., Z. Ren, D. Jia, and X. Wu (2009), Co-seismic thrusting rupture and slip distribution produced by the 2008  $i_i$   $m_i/i_i$   $sub_i$   $w_i/sub_i$  7.9 Wenchuan earthquake, China, *Tectonophysics*, 471(3), 203–215.

- Lisle, R. J. (2013), A critical look at the Wallace-Bott hypothesis in fault-slip analysis, *Bulletin de la Societe Geologique de France*, 184(4-5), 299–306.
- Liu, L., and M. D. Zoback (1992), The effect of topography on the state of stress in the crust: Application to the site of the Cajon Pass Scientific Drilling Project, *Journal of Geophysical Research: Solid Earth* (1978–2012), 97(B4), 5095–5108.
- Liu, M., and Y. Yang (2003), Extensional collapse of the Tibetan Plateau: Results of three-dimensional finite element modeling, *Journal of Geophysical Research: Solid Earth* (1978–2012), 108(B8).
- Liu-Zeng, J., Z. Zhang, L. Wen, P. Tappouer, J. Sun, X. Xing, G. Hu, Q. Xu, L. Zeng, L. Ding, et al. (2009), Co-seismic ruptures of the 12 may 2008, i<sub>i</sub>, m<sub>j</sub>, i<sub>i,j</sub>, sub<sub>i</sub>, s<sub>j</sub>/sub<sub>i</sub>, 8.0 wenchuan earthquake, sichuan: East–west crustal shortening on oblique, parallel thrusts along the eastern edge of tibet, *Earth and Planetary Science Letters*, 286(3), 355–370.
- Love, E. A. H. (1927), *The mathematical theory of elasticity*, Cambridge University Press.
- Loveless, J., and B. Meade (2011), Partitioning of localized and diffuse deformation in the Tibetan Plateau from joint inversions of geologic and geodetic observations, *Earth and Planetary Science Letters*, 303(1), 11–24.
- Luttrell, K., D. Sandwell, B. Smith-Konter, B. Bills, and Y. Bock (2007), Modulation of the earthquake cycle at the southern San Andreas fault by lake loading, *Journal of Geophysical Research: Solid Earth* (1978–2012), 112(B8).
- Luttrell, K. M., X. Tong, D. T. Sandwell, B. A. Brooks, and M. G. Bevis (2011), Estimates of stress drop and crustal tectonic stress from the 27 February 2010 Maule, Chile, earthquake: Implications for fault strength, *Journal of Geophysical Research: Solid Earth*, 116(B11).
- Martel, S. J. (2006), Effect of topographic curvature on near-surface stresses and application to sheeting joints, *Geophysical Research Letters*, 33(1).
- McKenzie, D. P. (1969), The relation between fault plane solutions for earthquakes and the directions of the principal stresses, *Bulletin of the Seismological Society of America*, 59(2), 591–601.
- McKinney, W. (2010), Data structures for statistical computing in python, in *Proceedings of the 9th Python in Science Conference*, edited by S. van der Walt and J. Millman, pp. 51–56, SciPy.
- McTigue, D. F., and C. C. Mei (1981), Gravity-induced stresses near topography of small slope, *Journal of Geophysical Research: Solid Earth*, 86(B10), 9268–9278.
- Meade, B. J., and C. P. Conrad (2008), Andean growth and the deceleration of South American subduction: Time evolution of a coupled orogen–subduction system, *Earth and Planetary Science Letters*, 275(1), 93–101.
- Medina Luna, L., and E. A. Hetland (2013), Regional stresses inferred from coseismic slip models of the 2008 Mw 7.9 Wenchuan, China, earthquake, *Tectonophysics*, 584, 43–53.
- Meissner, R., and J. Strehlau (1982), Limits of stresses in continental crusts and their relation to the depth-frequency distribution of shallow earthquakes, *Tectonics*, 1(1), 73–89.
- Michael, A. J. (1987), Use of focal mechanisms to determine stress: a control study, *Journal of Geophysical Research: Solid Earth* (1978–2012), 92(B1), 357–368.
- Miller, D. J., and T. Dunne (1996), Topographic perturbations of regional stresses and consequent bedrock fracturing, *Journal of Geophysical Research: Solid Earth* (1978–2012), 101(B11), 25,523–25,536.
- Molnar, P., and H. Lyon-Caen (1988), Some simple physical aspects of the support, structure, and evolution of mountain belts, *Spec. Pap. Geol. Soc. Am.*, 218, 179–207.
- Mosegaard, K., and A. Tarantola (1995), Monte Carlo sampling of solutions to inverse problems, *Journal of Geophysical Research: Solid Earth* (1978–2012), 100(B7), 12,431–12,447.
- Nakamura, T., S. Tsuboi, Y. Kaneda, and Y. Yamanaka (2010), Rupture process of the 2008 Wenchuan, China earthquake inferred from teleseismic waveform inversion and forward modeling of broadband seismic waves, *Tectonophysics*, 491(1), 72–84.
- Oglesby, D. D., and S. M. Day (2002), Stochastic fault stress: Implications for fault dynamics and ground motion, *Bulletin of the Seismological Society of America*, 92(8), 3006–3021.
- Oliphant, T. E. (2007), Python for scientific computing, *Computing in Science & Engineering*, 9(3), 10–20.
- Olsen, K., R. Madariaga, and R. Archuleta (1997), Three-dimensional dynamic simulation of the 1992 Landers earthquake, *Science*, 278(5339), 834–838.
- Pérez, F., and B. E. Granger (2007), IPython: a System for Interactive Scientific Computing, *Comput. Sci. Eng.*, 9(3), 21–29.
- Qi, W., Q. Xuejun, L. Qigui, J. Freymueller, Y. Shaomin, X. Caijun, Y. Yonglin, Y. Xinzhaoh, T. Kai, and C. Gang (2011), Rupture of deep faults in the 2008 Wenchuan earthquake and uplift of the Longmen Shan, *Nature Geoscience*, 4(9), 634–640.
- Reches, Z. (1987), Determination of the tectonic stress tensor from slip along faults that obey the coulomb yield condition, *Tectonics*, 6(6), 849–861.
- Rey, P., O. Vanderhaeghe, and C. Teyssier (2001), Gravitational collapse of the continental crust: definition, regimes and modes, *Tectonophysics*, 342(3), 435–449.
- Richardson, R. M., and D. D. Coblenz (1994), Stress modeling in the Andes: Constraints on the South American intraplate stress magnitudes, *Journal of Geophysical Research: Solid Earth*, 99(B11), 22,015–22,025.
- Savage, W. Z., and H. S. Swolfs (1986), Tectonic and gravitational stress in long symmetric ridges and valleys, *Journal of Geophysical Research: Solid Earth*, 91(B3), 3677–3685.
- Scholz, C. H. (2002), *The mechanics of earthquakes and faulting*, Cambridge university press.
- Seabold, S., and J. Perktold (2010), Statsmodels: econometric and statistical modeling with python, in *Proceedings of the 9th Python in Science Conference*, pp. 57–61, SciPy.
- Shen, Z.-K., J. Sun, P. Zhang, Y. Wan, M. Wang, R. Bürgmann, Y. Zeng, W. Gan, H. Liao, and Q. Wang (2009), Slip maxima at fault junctions and rupturing of barriers during the 2008 Wenchuan earthquake, *Nature Geoscience*, 2(10), 718–724.
- Sibson, R. H. (1985), A note on fault reactivation, *Journal of Structural Geology*, 7(6), 751–754.
- Styron, R., M. Taylor, and K. Okoronkwo (2010), Database of active structures from the Indo-Asian collision, *Eos, Transactions American Geophysical Union*, 91(20), 181–182.
- Tarantola, A. (2005), *Inverse problem theory and methods for model parameter estimation*, SIAM.
- Taylor, M., A. Yin, F. J. Ryerson, P. Kapp, and L. Ding (2003), Conjugate strike-slip faulting along the Bangong-Nujiang suture zone accommodates coeval east-west extension and north-south shortening in the interior of the Tibetan Plateau, *Tectonics*, 22(4).
- Tong, X., D. T. Sandwell, and Y. Fialko (2010), Coseismic slip model of the 2008 Wenchuan earthquake derived from joint inversion of interferometric synthetic aperture radar, GPS, and field data, *Journal of Geophysical Research: Solid Earth*, 115(B4).
- Townend, J., and M. D. Zoback (2000), How faulting keeps the crust strong, *Geology*, 28(5), 399–402.
- Wallace, R. E. (1951), Geometry of shearing stress and relation to faulting, *The Journal of Geology*, pp. 118–130.
- Wang, E., E. Kirby, K. P. Furlong, M. Van Soest, G. Xu, X. Shi, P. J. Kamp, and K. Hodges (2012), Two-phase growth of high topography in eastern Tibet during the Cenozoic, *Nature Geoscience*, 5(9), 640–645.
- Xiao, H.-B., F. Dahmen, and J. Suppe (1991), Mechanics of extensional wedges, *Journal of Geophysical Research: Solid Earth*, 96(B6), 10,301–10,318.
- Xu, X., X. Wen, G. Yu, G. Chen, Y. Klinger, J. Hubbard, and J. Shaw (2009), Coseismic reverse-and oblique-slip surface faulting generated by the 2008 mw 7.9 wenchuan earthquake, china, *Geology*, 37(6), 515–518.
- Yong, L., P. A. Allen, A. L. Densmore, and X. Qiang (2003), Evolution of the Longmen Shan foreland basin (western Sichuan, China) during the Late Triassic Indosinian orogeny, *Basin Research*, 15(1), 117–138.
- Zhang, G., C. Qu, X. Shan, X. Song, G. Zhang, C. Wang, J.-C. Hu, and R. Wang (2011), Slip distribution of the 2008 Wenchuan Ms 7.9 earthquake by joint inversion from GPS and InSAR measurements: a resolution test study, *Geophysical Journal International*, 186(1), 207–220.
- Zhang, P.-Z., X.-z. Wen, Z.-K. Shen, and J.-h. Chen (2010), Oblique, high-angle, listric-reverse faulting and associated development of strain: The Wenchuan earthquake of May 12, 2008, Sichuan, China, *Annual Review of Earth and Planetary Sciences*, 38, 353–382.

Corresponding author: Richard H. Styron, Department of Earth and Environmental Sciences, University of Michigan, 2534 CC Little Bldg., 1100 N. University Ave., Ann Arbor, MI 48104, USA (richard.h.styron@gmail.com)